Available online at www.sciencedirect.com
SCIENCE DIRECT®
Comput. Methods Appl. Mech. Engrg. 195 (2006) 3776–3796
Computer methods in applied mechanics and engineering
www.elsevier.com/locate/cma

Outflow boundary conditions for three-dimensional finite element modeling of blood flow and pressure in arteries

Irene E. Vignon-Clementel [a], C. Alberto Figueroa [a], Kenneth E. Jansen [c], Charles A. Taylor [a,b,*]

[a] *Department of Mechanical Engineering, Stanford University, E350 Clark Center, 318 Campus Drive, Stanford 94305-5431, CA 94305, USA*
[b] *Department of Bioengineering and Surgery, Stanford University, E350 Clark Center, 318 Campus Drive, Stanford 94305-5431, CA 94305, USA*
[c] *Scientific Computation Research Center and the Department of Mechanical, Aeronautical and Nuclear Engineering, Rensselaer Polytechnic Institute, Troy, NY 12180, USA*

Received 23 November 2004; received in revised form 8 February 2005; accepted 13 April 2005

Abstract

Flow and pressure waves emanate from the heart and travel through the major arteries where they are damped, dispersed and reflected due to changes in vessel caliber, tissue properties and branch points. As a consequence, solutions to the governing equations of blood flow in the large arteries are highly dependent on the outflow boundary conditions imposed to represent the vascular bed downstream of the modeled domain. The most common outflow boundary conditions for three-dimensional simulations of blood flow are prescribed constant pressure or traction and prescribed velocity profiles. However, in many simulations, the flow distribution and pressure field in the modeled domain are unknown and cannot be prescribed at the outflow boundaries. An alternative approach is to couple the solution at the outflow boundaries of the modeled domain with lumped parameter or one-dimensional models of the downstream domain. We previously described a new approach to prescribe outflow boundary conditions for simulations of blood flow based on the Dirichlet-to-Neumann and variational multiscale methods. This approach, termed the coupled multidomain method, was successfully applied to solve the non-linear one-dimensional equations of blood flow with a variety of models of the downstream domain. This paper describes the extension of this method to three-dimensional finite element modeling of blood flow and pressure in the major arteries. Outflow boundary conditions are derived for any downstream domain where an explicit relationship of pressure as a function of flow rate or velocities can be obtained at the coupling interface. We developed this method in the context of a stabilized, semi-discrete finite element method.

* Corresponding author. Address: Department of Mechanical Engineering, Stanford University, E350 Clark Center, 318 Campus Drive, Stanford, CA 94305, USA. Tel.: +1 650 725 6128; fax: +1 650 725 9082.
E-mail address: taylorca@stanford.edu (C.A. Taylor).

0045-7825/$ - see front matter
doi:10.1016/j.cma.2005.04.014

Flow rate and pressure distributions are shown for different boundary conditions to illustrate the dramatic influence of alternative boundary conditions on these quantities.

Keywords: Blood flow; Pressure; Boundary conditions; Coupled multidomain method; Finite elements

1. Introduction

In normal and disease states in children and adults, quantification of three-dimensional flow phenomena and pressure fields is important to understand the response of the cardiovascular system to biomechanical forces [1]. In the development of the circulatory system in normal subjects and congenital heart disease patients, flow modulates diameter and pressure controls wall thickness [2,3]. In older subjects, the initiation and progression of atherosclerotic and aneurismal disease is directly affected by the complex three-dimensional fluid mechanical environment of the major arteries [4,5]. Moreover, the ability to adequately simulate flow and pressure is needed to model the performance of devices such as heart valves, LVADs (left ventricular assist devices), filters, stents and stent-grafts. Non-invasive three-dimensional flow and pressure data can also provide important information to determine the significance of an obstruction or predict the outcome of a procedure [6,7].

In recent years, remarkable progress has been made in simulating blood flow in realistic anatomical models constructed from three-dimensional medical imaging data. Arguably, accurate anatomic models are of primary importance in simulating blood flow. However, as we demonstrate in this paper, realistic boundary conditions are equally important in computing velocity and pressure fields. Yet, this subject has received far less attention than image-based model construction for three-dimensional simulations. In contrast, significant progress has been made in devising outflow boundary conditions for solving the one-dimensional equations of blood flow in elastic vessels. For example, Stergiopulos solved the non-linear one-dimensional equations of blood flow in a comprehensive model of the arterial system using a lumped parameter model of the vasculature downstream of each branch in his numerical model [8]. Several groups have developed and analyzed the coupling of one-dimensional equations with lumped models [9–12]. In contrast to methods coupling the one-dimensional equations of blood flow to lumped parameter models, Olufsen developed a distributed downstream model based on calculating the input impedance of an asymmetric binary fractal tree using Womersley's linear wave theory [13,14] and an algorithm for computing the impedance of a vascular network first proposed by Taylor [15]. Olufsen's approach was to generate a fractal tree for each outlet starting from a vessel that matched the diameter of the outlet and diminished in size with each successive generation of vessels until a fixed terminal vessel size was attained. With this method an impedance for each outlet of the upstream numerical model was computed naturally from linear wave theory and branching laws. Olufsen's distributed model of the downstream vasculature enabled the representation of more realistic flow and pressure waveforms than those obtained with lumped parameter models [16]. Steele and Taylor used a modified version of Olufsen's impedance boundary condition to model blood flow at rest and during simulated exercise conditions [17]. In this case, vascular networks were assigned to the outlets of a model of the abdominal aorta, modified to represent the resting flow distribution of 11 different subjects and then dilated to simulate the effects of lower limb exercise. Vignon and Taylor developed a multidomain approach to couple one-dimensional equations to different lumped and one-dimensional boundary conditions [18]. While these one-dimensional methods can be used to compute flow rate and mean pressure, by design, they cannot be used to simulate complex three-dimensional flow phenomena and pressure losses. Three-dimensional numerical methods have been used to compute velocity fields and quantify shear forces acting on the surface of blood vessels. However, since most three-dimensional models of blood flow use zero or constant pressure, zero traction, or prescribed velocity profiles

as outlet boundary conditions, blood pressure is not computed accurately and notably absent from reports of hemodynamic investigations [19–24].

For simulations of blood flow in large arteries, the outlet boundary conditions represent the downstream vasculature including smaller arteries, arterioles, capillaries, venules and veins returning blood to the heart. Clearly, the vast extent and complexity of the circulation precludes a three-dimensional representation of the entire circuit, yet ignoring the effect of the downstream circulation results in grossly inaccurate predictions of velocity and pressure fields for many problems where the distribution of flow between the major arteries is unknown. If zero or equal pressures or tractions are used for different outlets, the flow split will be dictated solely by the resistance to flow in the branches of the domain of interest, neglecting the dominant effect of the resistance of the downstream vascular beds. An alternative approach is to utilize three-dimensional models for the major arteries where high-fidelity information is needed, and reduced-order models to represent the remainder of the system. While closed-loop models are optimal, a simpler approach is to directly represent the vasculature of the small arteries and arterioles using zero-dimensional or one-dimensional models. These models can be terminated at the level of the capillary vessels where an assumption of constant pressure is reasonable. Several groups [6,25–33] have successfully coupled three-dimensional models to either resistances or more sophisticated zero-dimensional models (lumped models), but this coupling has been performed iteratively, and generally applied to geometries with few outlets and low resistances (as seen in the pulmonary vasculature). A further limitation of these methods to couple three-dimensional and zero-dimensional models is the fact that there is no direct relationship between the anatomy of the downstream vascular bed and the lumped parameters resulting in difficulties in specifying these parameters and relating them to subsequent physiologic or pathophysiologic changes in the downstream vasculature. In addition, for many simulations based on three-dimensional imaging data, anatomic information is available for vessels downstream of the primary region of interest. The incorporation of such data would improve the accuracy of the models of the downstream vasculature.

Methods to couple three-dimensional and one-dimensional models were first described by Formaggia et al. [34,35]. While great progress was made in these landmark papers, the coupling was performed for simple geometries and iteratively. Based on our experience, implicit coupling significantly improves convergence, especially for models with multiple outlets. In addition, these papers did not include coupling between three-dimensional domains and complex vascular networks as have been incorporated in one-dimensional numerical solutions of blood flow in arteries. Since the vascular bed from the major arteries to the capillaries can include tens of millions of blood vessels, non-linear one-dimensional models would be intractable. However, using linear wave propagation theory the input impedance of the downstream vascular bed can be computed for large complex vascular trees. A method to prescribe the impedance (calculated using linear wave theory) of these downstream vascular beds at the outlets of three-dimensional models would enable the specification of realistic boundary conditions for three-dimensional simulations of blood flow and pressure.

While inadequate outflow boundary conditions and rigid-wall models are the main impediments to the realistic prediction of pressure in three-dimensional blood flow simulations, in this paper we focus on the first issue and do not address the issue of wall deformability in the three-dimensional domain. We describe a new method to prescribe outflow boundary conditions in the context of the finite element method as this method is particularly well suited for handling complex geometries and boundary conditions inherent in modeling blood flow [24]. The approach we describe is based on the Dirichlet-to-Neumann (DtN) [36] and the variational multiscale [37] methods and is an extension of the 1D coupled multidomain approach we successfully applied with a variety of models of the downstream domain [18]. For one-dimensional problems, we demonstrated that a DtN map can be calculated for the impedance of complex vascular trees and that this approach incorporates naturally occurring wave reflections from a downstream bed. Wave propagation in transient and periodic states was simulated and the importance of selecting appropriate boundary conditions was demonstrated for one-dimensional simulations of blood flow. We also noted that the

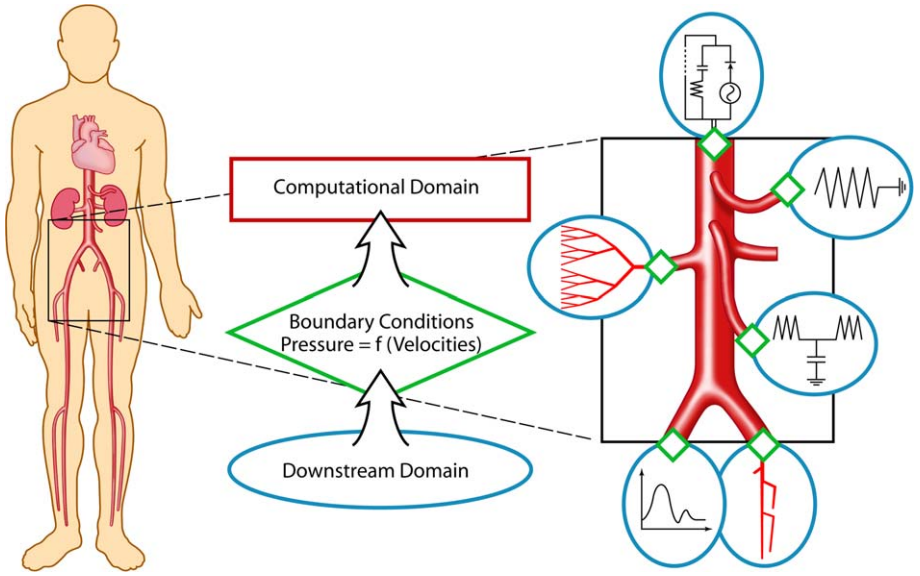

Fig. 1. Illustration of the "Coupled Multidomain Method", where information from the downstream (analytical) domain is incorporated in the upstream (computational) domain through a boundary map. This approach accommodates a variety of downstream models ranging from pure resistive to complex electrical analogs and impedance models.

best boundary condition for cardiovascular applications is not the one that exhibits no wave reflection, since wave reflections naturally arising from downstream beds (from bifurcations, tapering, and variations in wall properties) should propagate back upstream into the numerical domain. We concluded that, at present, impedance-based boundary conditions are the best approach for incorporating natural sites of wave reflection in the downstream vasculature.

In this paper we present a coupled multidomain approach for three-dimensional finite element simulations of blood flow and pressure. Given the computational expense of three-dimensional numerical methods and the resolution limits imposed by current imaging technologies, we constrain the three-dimensional domain to the major arteries, and model the downstream domains with simpler models (Fig. 1). The outlet boundary conditions are implemented implicitly resulting in good stability and convergence properties at physiologic pressures. The organization of the paper will begin with the description of our coupled multidomain method in three-dimensions and its specialization to resistance and impedance boundary conditions. We then demonstrate this new method on a straight, cylindrical blood vessel, a bifurcation model with a stenosis on one side, and a subject-specific model of the human abdominal aorta.

2. Methods

2.1. Governing equations (strong form)

The method described can be applied to conservative as well as advective formulations of the incompressible Navier–Stokes equations, and was successfully implemented in both cases. We proceed by defining the spatial domain as Ω and its boundary as Γ. The three-dimensional equations for the flow of an incompressible Newtonian fluid consist of the three momentum balance equations and the continuity equation (written here in advective form) subject to suitable initial and boundary conditions

$$\begin{aligned}
&\rho\vec{v}_{,t} + \rho\vec{v}\cdot\nabla\vec{v} = -\nabla p + \operatorname{div}(\underset{\sim}{\tau}) + \vec{f}\\
&\operatorname{div}(\vec{v}) = 0\\
&\underset{\sim}{\tau} = 2\mu\underset{\sim}{D} \quad \text{with } \underset{\sim}{D} = \frac{1}{2}(\nabla\vec{v} + \nabla\vec{v}^{\mathrm{T}}).
\end{aligned} \tag{1}$$

The primary variables are the fluid velocity $\vec{v} = (v_x, v_y, v_z)$ and the pressure p. The density of the fluid is given by ρ (assumed constant), the external force by $\vec{f}$, and the viscosity by μ (assumed constant).

In regards to boundary conditions, the boundary Γ of the spatial domain can be split into a Dirichlet partition Γ_g and a Neumann partition Γ_h such that ($\Gamma = \partial\Omega = \Gamma_g \cup \Gamma_h; \Gamma_g \cap \Gamma_h = \emptyset$). Considering this, the velocity at the inlet(s) of the domain is typically specified as

$$\vec{v}(\vec{x}, t) = \vec{v}^{\text{in}}(\vec{x}, t) \quad \vec{x} \in \Gamma^{\text{in}} \subset \Gamma_g. \tag{2}$$

A no-slip boundary condition is imposed on the walls (surfaces that are neither inlets nor outlets). We discuss outflow boundary conditions subsequently. The initial conditions for this problem are given by

$$\vec{v}(\vec{x}, 0) = \vec{v}^{0}(\vec{x}) \quad \vec{x} \in \Omega. \tag{3}$$

2.2. Weak form

We define the trial solution and weighting function spaces for the semi-discrete formulation as

$$\begin{aligned}
&\mathscr{S} = \{\vec{v} | \vec{v}(\cdot, t) \in H^1(\Omega)^{n_{\text{sd}}}, t \in [0, T], \vec{v}(\cdot, t) = \vec{g} \quad \text{on } \Gamma_g\},\\
&\mathscr{W} = \{\vec{w} | \vec{w}(\cdot, t) \in H^1(\Omega)^{n_{\text{sd}}}, t \in [0, T], \vec{w}(\cdot, t) = \vec{0} \quad \text{on } \Gamma_g\},\\
&\mathscr{P} = \{p | p(\cdot, t) \in H^1(\Omega), t \in [0, T]\},
\end{aligned} \tag{4}$$

where H^1 represents the usual Sobolev space of functions with square-integrable values and first derivatives in Ω; n_{sd} represents the number of spatial dimensions and $\vec{g}$ represents the prescribed Dirichlet boundary condition.

The weak form reads: find $\vec{v} \in \mathscr{S}$ and $p \in \mathscr{P}$ such that for every $\vec{w} \in \mathscr{W}$ and $q \in \mathscr{P}$

$$\begin{aligned}
&B_G(\vec{w}, q; \vec{v}, p) = 0,\\
&B_G(\vec{w}, q; \vec{v}, p) = \int_\Omega \left\{\vec{w}\cdot(\rho\vec{v}_{,t} + \rho\vec{v}\cdot\nabla\vec{v} - \vec{f}) + \nabla\vec{w} : (-p\underset{\sim}{I} + \underset{\sim}{\tau})\right\} \mathrm{d}\vec{x}\\
&\qquad\qquad - \int_\Omega \nabla q \cdot \vec{v}\,\mathrm{d}\vec{x} - \int_{\Gamma_h} \vec{w}\cdot(-p\underset{\sim}{I} + \underset{\sim}{\tau})\cdot\vec{n}\,\mathrm{d}s + \int_\Gamma q\vec{v}\cdot\vec{n}\,\mathrm{d}s.
\end{aligned} \tag{5}$$

2.3. Coupled multidomain method

We adopt the following approach to derive appropriate outflow boundary conditions [18,37]. First, we divide the spatial domain Ω into an upstream "numerical" domain $\widehat{\Omega}$, and a downstream "analytic" domain Ω' such that $\widehat{\Omega} \cap \Omega' = \emptyset$ and $\overline{\widehat{\Omega} \cup \Omega'} = \Omega$. The boundary that separates these domains is defined as Γ_B (Fig. 2). We define a disjoint decomposition of the variables, for example for the unknown solution vector, $\boldsymbol{U}(\vec{x}, t) = [\vec{v}, p]^{\mathrm{T}}$, $(\vec{x}, t) \in \Omega \times [0, T]$,

$$\boldsymbol{U} = \widehat{\boldsymbol{U}} + \boldsymbol{U}' \quad \text{with } \widehat{\boldsymbol{U}}|_{\Omega'} = \boldsymbol{0} \quad \text{and} \quad \boldsymbol{U}'|_{\hat{\Omega}} = \boldsymbol{0} \tag{6}$$

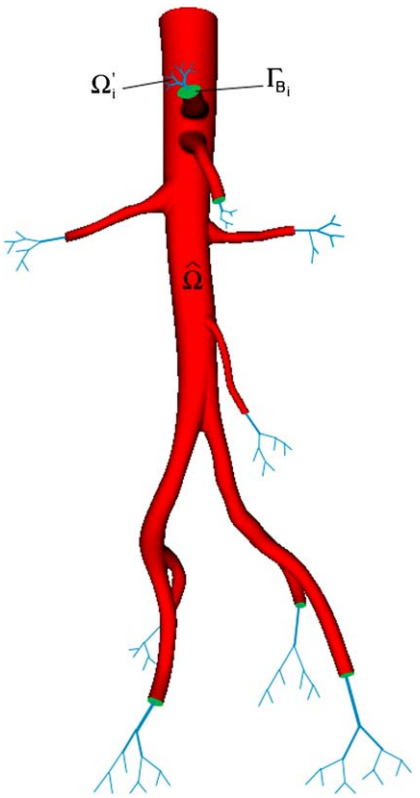

Fig. 2. The spatial domain is divided between the upstream numerical domain $\widehat{\Omega}$ (main model) and the downstream analytic domain $\widehat{\Omega} = \cup_i \Omega_i'$ (here the trees), separated by the coupling boundary $\Gamma_B = \cup_i \Gamma_{B_i}$ (here in green).

so that

$$\boldsymbol{U} = \left\{ \widehat{\boldsymbol{U}} | \vec{x} \in \widehat{\Omega}, \quad \boldsymbol{U}' | \vec{x} \in \Omega' \quad \text{and} \quad \widehat{\boldsymbol{U}} = \boldsymbol{U}' \ \vec{x} \in \Gamma_B \right\}. \tag{7}$$

Note also that

$$\vec{n}' = -\hat{\vec{n}}. \tag{8}$$

We use a similar decomposition for the weighting functions, and insert these expressions into the previous variational form:

$$\begin{aligned} &\int_\Omega (\hat{\vec{w}} + \vec{w}') \cdot \left(\rho(\hat{\vec{v}}_{,t} + \vec{v}'_{,t}) + \rho(\hat{\vec{v}} + \vec{v}') \cdot \nabla(\hat{\vec{v}} + \vec{v}') - \vec{f} \right) + (\nabla \hat{\vec{w}} + \nabla \vec{w}') : \left(-(\hat{p} + p') \underset{\sim}{I} + (\hat{\tau} + \tau') \right) \mathrm{d}\vec{x} \\ &\quad - \int_{\Gamma_h} (\hat{\vec{w}} + \vec{w}') \cdot \left(-(\hat{p} + p') \underset{\sim}{I} + (\underset{\sim}{\hat{\tau}} + \underset{\sim}{\tau}') \right) \cdot \vec{n} \, \mathrm{d}s - \int_\Omega (\nabla \hat{q} + \nabla q') \cdot (\hat{\vec{v}} + \vec{v}') \, \mathrm{d}\vec{x} \\ &\quad + \int_\Gamma (\hat{q} + q')(\hat{\vec{v}} + \vec{v}') \cdot \vec{n} \, \mathrm{d}s = 0. \end{aligned} \tag{9}$$

The disjoint nature of this expression is used to derive a new variational form for the numerical domain. Specifically, since $\widehat{\boldsymbol{U}}$ vanishes on Ω' and $\boldsymbol{U}'$ vanishes on $\widehat{\Omega}$ (and similarly for the weighting functions), we find:

$$\int_{\hat{\Omega}} \hat{\vec{w}} \cdot (\rho \hat{\vec{v}}_{,t} + \rho \hat{\vec{v}} \cdot \nabla \hat{\vec{v}} - \hat{\vec{f}}) + \nabla \hat{\vec{w}} : (-\hat{p} \underset{\sim}{I} + \hat{\underset{\sim}{\tau}}) \, \mathrm{d}\vec{x} - \int_{\hat{\Gamma}_h} \hat{\vec{w}} \cdot (-\hat{p} \underset{\sim}{I} + \hat{\underset{\sim}{\tau}}) \cdot \hat{\vec{n}} \, \mathrm{d}s$$
$$+ \int_{\Omega'} \vec{w}' \cdot (\rho \vec{v}'_{,t} + \rho \vec{v}' \cdot \nabla \vec{v}' - \vec{f}) + \nabla \vec{w}' : (-p' \underset{\sim}{I} + \underset{\sim}{\tau}') \, \mathrm{d}\vec{x} - \int_{\Gamma'_h} \vec{w}' \cdot (-p' \underset{\sim}{I} + \underset{\sim}{\tau}') \cdot \vec{n}' \, \mathrm{d}s - \int_{\hat{\Omega}} \nabla \hat{q} \cdot \hat{\vec{v}} \, \mathrm{d}\vec{x}$$
$$+ \int_{\hat{\Gamma}} \hat{q} \hat{\vec{v}} \cdot \hat{\vec{n}} \, \mathrm{d}s - \int_{\Omega'} \nabla q' \cdot \vec{v}' \, \mathrm{d}\vec{x} + \int_{\Gamma'} q' \vec{v}' \cdot \vec{n}' \, \mathrm{d}s = 0. \tag{10}$$

Now since (1) holds in Ω', we obtain the original variational form specialized to the numerical domain $\widehat{\Omega}$ with the addition of boundary terms accounting for the interface to the analytic domain, Ω'

$$\int_{\hat{\Omega}} \hat{\vec{w}} \cdot (\rho \hat{\vec{v}}_{,t} + \rho \hat{\vec{v}} \cdot \nabla \hat{\vec{v}} - \hat{\vec{f}}) + \nabla \hat{\vec{w}} : (-\hat{p} \underset{\sim}{I} + \hat{\underset{\sim}{\tau}}) \, \mathrm{d}\vec{x} - \int_{\hat{\Gamma}_h} \hat{\vec{w}} \cdot (-\hat{p} \underset{\sim}{I} + \hat{\underset{\sim}{\tau}}) \cdot \hat{\vec{n}} \, \mathrm{d}s$$
$$+ \int_{\Gamma_B} \vec{w}' \cdot (-p' \underset{\sim}{I} + \underset{\sim}{\tau}') \cdot \vec{n}' \, \mathrm{d}s - \int_{\hat{\Omega}} \nabla \hat{q} \cdot \hat{\vec{v}} \, \mathrm{d}\vec{x} + \int_{\hat{\Gamma}} \hat{q} \hat{\vec{v}} \cdot \hat{\vec{n}} \, \mathrm{d}s - \int_{\Gamma_B} q' \vec{v}' \cdot \vec{n}' \, \mathrm{d}s = 0. \tag{11}$$

Here we introduce an approximation to be able to quantify the terms above that come from the downstream domain:

$$\begin{aligned} (-p' \underset{\sim}{I} + \underset{\sim}{\tau}')|_{\Gamma_B} &\approx [\underset{\sim}{M}_m(\vec{v}', p') + \underset{\sim}{H}_m]_{\Gamma_B}, \\ \vec{v}'|_{\Gamma_B} &\approx [\vec{M}_c(\vec{v}', p') + \vec{H}_c]_{\Gamma_B}. \end{aligned} \tag{12}$$

The operators $\boldsymbol{M} = [\underset{\sim}{M}_m, \vec{M}_c]_{\Gamma_B}$ and $\boldsymbol{H} = [\underset{\sim}{H}_m, \vec{H}_c]_{\Gamma_B}$ are defined on the Ω' domain based on the chosen model to represent the downstream domain (different examples are provided subsequently).

Then using Eqs. (7) and (8), we enforce the continuity of the momentum and mass fluxes across Γ_B

$$\begin{aligned} \int_{\Gamma_B} \hat{\vec{w}} \cdot (\underset{\sim}{M}_m(\hat{\vec{v}}, \hat{p}) + \underset{\sim}{H}_m) \cdot \hat{\vec{n}} \, \mathrm{d}s &= -\int_{\Gamma_B} \vec{w}' \cdot (\underset{\sim}{M}_m(\vec{v}', p') + \underset{\sim}{H}_m) \cdot \vec{n}' \, \mathrm{d}s, \\ \int_{\Gamma_B} \hat{q} (\vec{M}_c(\hat{\vec{v}}, \hat{p}) + \vec{H}_c) \cdot \hat{\vec{n}} \, \mathrm{d}s &= -\int_{\Gamma_B} q' (\vec{M}_c(\vec{v}', p') + \vec{H}_c) \cdot \vec{n}' \, \mathrm{d}s. \end{aligned} \tag{13}$$

We thus approximate the boundary terms on Γ_B in the weak form (11) by

$$\begin{aligned} \int_{\Gamma_B} \vec{w}' \cdot (-p' \underset{\sim}{I} + \underset{\sim}{\tau}') \cdot \vec{n}' \, \mathrm{d}s &\approx -\int_{\Gamma_B} \hat{\vec{w}} \cdot (\underset{\sim}{M}_m(\hat{\vec{v}}, \hat{p}) + \underset{\sim}{H}_m) \cdot \hat{\vec{n}} \, \mathrm{d}s, \\ \int_{\Gamma_B} q' \vec{v}' \cdot \vec{n}' \, \mathrm{d}s &\approx -\int_{\Gamma_B} \hat{q} (\vec{M}_c(\hat{\vec{v}}, \hat{p}) + \vec{H}_c) \cdot \hat{\vec{n}} \, \mathrm{d}s. \end{aligned} \tag{14}$$

The resulting weak form for the multidomain method is then

$$\int_{\hat{\Omega}} \hat{\vec{w}} \cdot (\rho \hat{\vec{v}}_{,t} + \rho \hat{\vec{v}} \cdot \nabla \hat{\vec{v}} - \hat{\vec{f}}) + \nabla \hat{\vec{w}} : (-\hat{p} \underset{\sim}{I} + \hat{\underset{\sim}{\tau}}) \, \mathrm{d}\vec{x} - \int_{\hat{\Gamma}_h} \hat{\vec{w}} \cdot (-\hat{p} \underset{\sim}{I} + \hat{\underset{\sim}{\tau}}) \cdot \hat{\vec{n}} \, \mathrm{d}s,$$
$$\boxed{-\int_{\Gamma_B} \hat{\vec{w}} \cdot (\underset{\sim}{M}_m(\hat{\vec{v}}, \hat{p}) + \underset{\sim}{H}_m) \cdot \hat{\vec{n}} \, \mathrm{d}s} - \int_{\hat{\Omega}} \nabla \hat{q} \cdot \hat{\vec{v}} \, \mathrm{d}\vec{x} + \int_{\hat{\Gamma}} \hat{q} \hat{\vec{v}} \cdot \hat{\vec{n}} \, \mathrm{d}s + \boxed{\int_{\Gamma_B} \hat{q} (\vec{M}_c(\hat{\vec{v}}, \hat{p}) + \vec{H}_c) \cdot \hat{\vec{n}} \, \mathrm{d}s} = 0. \tag{15}$$

We see that the solution in the numerical domain depends on operators defined by the mathematical model chosen to represent the physics of the downstream domain (see the terms in boxes) but not the solution variable, $\vec{v}'$ and p' in the downstream domain.

2.4. Derivation of the operators depending on the model chosen to represent the physics in the downstream domain

In selecting a mathematical model of the downstream domain Ω', we have the goal of obtaining a representation formula whereby the solution on the boundary Γ_B can be obtained as a function of the problem on the interior of the analytic domain and the outlet(s) of the analytic domain. Fundamentally, this representation formula will depend on the approximations we introduce in treating the downstream domain. We consider two possibilities, namely zero-dimensional models and one-dimensional wave propagation theory. In those cases, we will have a relationship between mean pressure and flow rate at Γ_B, but this method can incorporate more general relationships between the primary variables or functions of them—namely, full traction relationships instead of just the normal component.

2.4.1. Resistance boundary condition

We first present the results for the simplest zero-dimensional model for the downstream domain, the resistance. The general concept of resistance is to define a constant relationship between mean pressure and flow rate $P = QR$ [38], consistent with Poiseuille flow where the flow is fully developed (gradients in the axial direction are zero). We make the assumption that pressure in the downstream domain is constant over the cross-sectional area of the inlet boundary Γ_B so that

$$p' - \vec{n}' \cdot \underset{\sim}{\tau}' \cdot \vec{n}' = p' - 0 = \frac{\int_{\Gamma_B} p' \,\mathrm{d}s}{\int_{\Gamma_B} \mathrm{d}s} = -R \int_{\Gamma_B} \vec{v}' \cdot \vec{n}' \,\mathrm{d}s. \tag{16}$$

Therefore, the operators $\boldsymbol{M}$ and $\boldsymbol{H}$ are defined as

$$\begin{aligned} &[\underset{\sim}{M}_m(\vec{v}', p') + \underset{\sim}{H}_m]_{\Gamma_B} = \left(R \int_{\Gamma_B} \vec{v}' \cdot \vec{n}' \,\mathrm{d}s \, \underset{\sim}{I} + \underset{\sim}{\tau}' - \vec{n}' \cdot \underset{\sim}{\tau}' \cdot \vec{n}' \, \underset{\sim}{I} \right)\Big|_{\Gamma_B}, \\ &[\vec{M}_c(\vec{v}', p') + \vec{H}_c]_{\Gamma_B} = \vec{v}'|_{\Gamma_B}. \end{aligned} \tag{17}$$

Note that the sign of the resistance part of the operators changes if the face is an inlet or an outlet. Here, Γ_B is an inlet for Ω' and an outlet for $\widehat{\Omega}$. In this simple resistance case, the first box representing a term on the coupling interface Γ_B in (15) is modified as follows:

$$\int_{\Gamma_B} \hat{\vec{w}} \cdot (\underset{\sim}{M}_m(\hat{\vec{v}}, \hat{p}) + \underset{\sim}{H}_m) \cdot \hat{\vec{n}} \,\mathrm{d}s = -\int_{\Gamma_B} \hat{\vec{w}} \cdot \hat{\vec{n}} \left(R \int_{\Gamma_B} \hat{\vec{v}} \cdot \hat{\vec{n}} \,\mathrm{d}s + \hat{\vec{n}} \cdot \underset{\sim}{\hat{\tau}} \cdot \hat{\vec{n}} \right) \mathrm{d}s + \int_{\Gamma_B} \hat{\vec{w}} \cdot \underset{\sim}{\hat{\tau}} \cdot \hat{\vec{n}} \,\mathrm{d}s. \tag{18}$$

2.4.2. Impedance boundary condition

An example of a memory map is the impedance model, which is analogous to the concept of *impedance* in electricity. In this paper the downstream domain is approximated using Womersley's linear wave theory [13,14] in an asymmetric fractal tree to derive a one-dimensional impedance $Z(t)$ assuming periodicity in time. Note that in this theory $\vec{n} \cdot \underset{\sim}{\tau} \cdot \vec{n}$ is negligible. We can then derive for an inlet face:

$$\begin{aligned} p' - \vec{n}' \cdot \underset{\sim}{\tau}' \cdot \vec{n}' \approx p' - 0 &= \frac{\int_{\Gamma_B} p' \,\mathrm{d}s}{\int_{\Gamma_B} \mathrm{d}s} = -\frac{1}{T} \int_{t-T}^{t} Z(t - t_1) q'(t_1) \,\mathrm{d}t_1 \\ &= -\frac{1}{T} \int_{t-T}^{t} Z(t - t_1) \int_{\Gamma_B} \vec{v}'(t_1) \cdot \vec{n}' \,\mathrm{d}s \,\mathrm{d}t_1. \end{aligned} \tag{19}$$

The flow rate at time t depends on the history of the pressure over one period. The representation formula for the operators is obtained as

$$[\underset{\sim}{M}_m(\vec{v}',p') + \underset{\sim}{H}_m]_{\Gamma_B} = \left(\frac{1}{T}\int_{t-T}^{t} Z(t-t_1)\int_{\Gamma_B} \vec{v}'(t_1)\cdot\vec{n}'\,\mathrm{d}s\,\mathrm{d}t_1\,\underset{\sim}{I} + \underset{\sim}{\tau}' - \vec{n}'\cdot\underset{\sim}{\tau}'\cdot\vec{n}'\,\underset{\sim}{I}\right)\Big|_{\Gamma_B},$$
$$[\vec{M}_c(\vec{v}',p') + \vec{H}_c]_{\Gamma_B} = \vec{v}'|_{\Gamma_B}. \tag{20}$$

As before, note that the sign of the impedance part of the operators changes if the face is an inlet or an outlet. Here, Γ_B is an inlet for Ω' and an outlet for $\hat{\Omega}$. For this memory case, the first box on the coupling interface Γ_B in (15) is modified as follows:

$$\int_{\Gamma_B} \hat{\vec{w}}\cdot(\underset{\sim}{M}_m(\hat{\vec{v}},\hat{p}) + \underset{\sim}{H}_m)\cdot\hat{\vec{n}}\,\mathrm{d}s = -\int_{\Gamma_B}\hat{\vec{w}}\cdot\hat{\vec{n}}\left(\frac{1}{T}\int_{t-T}^{t} Z(t-t_1)\int_{\Gamma_B}\hat{\vec{v}}(t_1)\cdot\hat{\vec{n}}\,\mathrm{d}s\,\mathrm{d}t_1 + \hat{\vec{n}}\cdot\underset{\sim}{\hat{\tau}}\cdot\hat{\vec{n}}\right)\mathrm{d}s + \int_{\Gamma_B}\hat{\vec{w}}\cdot\underset{\sim}{\hat{\tau}}\cdot\hat{\vec{n}}\,\mathrm{d}s. \tag{21}$$

Remark 1. Pressure and velocities on the boundary become unknown solution variables. Thus this method enforces an implicitly coupled boundary condition.

Remark 2. The method described above can also be used when the impedance is derived from a (zero-dimensional) lumped parameter model.

Remark 3. The components of the natural boundary integrals over Γ_h in (5) that are not explicitly described above in (18) and (21) are computed directly from the current solution

$$\int_{\Gamma_B}\hat{\vec{w}}\cdot\underset{\sim}{\hat{\tau}}\cdot\hat{\vec{n}} - \hat{\vec{w}}\cdot\hat{\vec{n}}(\hat{\vec{n}}\cdot\underset{\sim}{\hat{\tau}}\cdot\hat{\vec{n}})\,\mathrm{d}s. \tag{22}$$

These so-called "consistent boundary conditions" are not in fact boundary conditions since they are directly computed from the solution variables. For a description of this as well as many alternative outflow boundary conditions see Gresho and Sani [39]. In particular, the magnitude of the tangential tractions which arise in Eqs. (18) and (21) are very small relative to other terms and could be neglected with minimal effect on accuracy and stability.

Remark 4. For simplicity, we omit the $\wedge$ superscript from the field variables and the corresponding spaces in the subsequent sections.

2.5. Finite element discretization

We employ a stabilized semi-discrete finite element method, based on ideas developed in Brooks and Hughes [40], Franca and Frey [41], Taylor et al. [24]. The discrete trial solution and weighting function spaces for the semi-discrete formulation are given by

$$\begin{aligned}
\mathcal{S}_h^k &= \{\vec{v}|\vec{v}(\cdot,t)\in H^1(\Omega)^{n_{\mathrm{sd}}}, t\in[0,T], \vec{v}|_{\vec{x}\in\overline{\Omega}_e}\in P_k(\overline{\Omega}_e)^{n_{\mathrm{sd}}}, \vec{v}(\cdot,t)=\hat{\vec{g}} \text{ on } \Gamma_g\},\\
\mathcal{W}_h^k &= \{\vec{w}|\vec{w}(\cdot,t)\in H^1(\Omega)^{n_{\mathrm{sd}}}, t\in[0,T], \vec{w}|_{x\in\overline{\Omega}_e}\in P_k(\overline{\Omega}_e)^{n_{\mathrm{sd}}}, \vec{w}(\cdot,t)=\vec{0} \text{ on } \Gamma_g\},\\
\mathcal{P}_h^k &= \{p|p(\cdot,t)\in H^1(\Omega), t\in[0,T], p|_{x\in\overline{\Omega}_e}\in P_k(\bar{\Omega}_e)\}.
\end{aligned} \tag{23}$$

Considering this, the weak form becomes: find $\vec{v}\in\mathcal{S}_h^k$ and $p\in\mathcal{P}_h^k$ such that for every $\vec{w}\in\mathcal{W}_h^k$ and $q\in\mathcal{P}_h^k$

$$
\begin{aligned}
&B_G(\vec{w},q;\vec{v},p) = 0,\\
&B_G(\vec{w},q;\vec{v},p) = \int_\Omega \{\vec{w}\cdot(\rho\vec{v}_{,t} + \rho\vec{v}\cdot\nabla\vec{v} - \vec{f}) + \nabla\vec{w} : (-p\underset{\sim}{I} + \underset{\sim}{\tau})\}\,\mathrm{d}\vec{x} - \int_\Omega \nabla q\cdot\vec{v}\,\mathrm{d}\vec{x}\\
&\qquad - \int_{\Gamma_h} \vec{w}(-p\underset{\sim}{I} + \underset{\sim}{\tau})\vec{n}\,\mathrm{d}s + \int_{\Gamma-\Gamma_B} q\vec{v}\cdot\vec{n}\,\mathrm{d}s\\
&\qquad \boxed{- \int_{\Gamma_B} \vec{w}(\underset{\sim}{M}_m(\vec{v},p) + \underset{\sim}{H}_m)\cdot\vec{n}\,\mathrm{d}\Gamma + \int_{\Gamma_B} q(\vec{M}_c(\vec{v},p) + \vec{H}_c)\cdot\vec{n}\,\mathrm{d}\Gamma}.
\end{aligned}
\tag{24}
$$

In this equation, the superscripts h, k of the discrete approximation of the continuous variables have been omitted for simplicity. Note that the boundary terms are identified in the box. In order to stabilize the Galerkin method, the formulation becomes [24,42]:

Find $\vec{v}\in\mathscr{S}_h^k$ and $p\in\mathscr{P}_h^k$ such that for every $\vec{w}\in\mathscr{W}_h^k$ and $q\in\mathscr{P}_h^k$

$$
\begin{aligned}
&B(\vec{w},q;\vec{v},p) = 0,\\
&B(\vec{w},q;\vec{v},p) = B_G(\vec{w},q;\vec{v},p) \;+\; \sum_{e=1}^{n_{el}} \int_{\overline{\Omega}_e} \{(\vec{v}\cdot\nabla)\vec{w}\cdot\tau_M\vec{\mathscr{L}}(\vec{v},p) + \nabla\cdot\vec{w}\tau_C\nabla\cdot\vec{v}\}\,\mathrm{d}\vec{x}\\
&\qquad + \sum_{e=1}^{n_{el}} \int_{\overline{\Omega}_e} \{\vec{w}\cdot(\rho\overset{\Delta}{\vec{v}}\cdot\nabla\vec{v}) + (\vec{\mathscr{L}}(\vec{v},p)\cdot\nabla\vec{w})\cdot(\bar{\tau}\vec{\mathscr{L}}(\vec{v},p)\cdot\nabla\vec{v})\}\,\mathrm{d}\vec{x}\\
&\qquad + \sum_{e=1}^{n_{el}} \int_{\overline{\Omega}_e} \nabla q\cdot\frac{\tau_M}{\rho}\vec{\mathscr{L}}(\vec{v},p)\,\mathrm{d}\vec{x},
\end{aligned}
\tag{25}
$$

$\vec{\mathscr{L}}(\vec{v},p)$ represents the residual vector of the momentum equation:

$$
\vec{\mathscr{L}}(\vec{v},p) = \rho\vec{v}_{,t} + \rho\vec{v}\cdot\nabla\vec{v} + \nabla p - \nabla\cdot\underset{\sim}{\tau} - \vec{f}. \tag{26}
$$

And $\overset{\Delta}{\vec{v}}$ is a conservation-restoring advective velocity whose expression is given by

$$
\overset{\Delta}{\vec{v}} = -\frac{\tau_M}{\rho}\vec{\mathscr{L}}(\vec{v},p). \tag{27}
$$

The stabilization parameters are defined as follows:

$$
\begin{aligned}
&\tau_M = \frac{1}{\sqrt{(2c_1/\Delta t)^2 + \vec{v}\cdot\underset{\sim}{g}\,\vec{v} + c_2 v^2(\underset{\sim}{g} : \underset{\sim}{g} + \omega^2)}},\\
&\tau_C = \frac{\rho}{8\tau_M \mathrm{tr}(\underset{\sim}{g})}\frac{C_{\tau_C}}{c_1} \quad\text{and}\quad \bar{\tau} = \frac{\tau_M}{\sqrt{\vec{\mathscr{L}}(\vec{v},p)\cdot\underset{\sim}{g}\cdot\vec{\mathscr{L}}(\vec{v},p)}},
\end{aligned}
\tag{28}
$$

where c_1 and c_2 are constants defined from the one-dimensional scalar model problem of the advection–diffusion equation. ω is the frequency of rotation of the reference frame, C_{τ_C} is a scale factor for τ_C, and $\underset{\sim}{g}$ is the covariant metric tensor

$$
\underset{\sim}{g} = (\vec{\xi}_{,\vec{x}})^{\mathrm{T}}\vec{\xi}_{,\vec{x}}. \tag{29}
$$

These non-linear equation (25) are then solved using methods described in [42,43]. The "coupled multi-domain method" was implemented for different boundary conditions in both the advective and the conservative forms, explicitly (in the residual only) and implicitly (in both the tangent matrix and the residual). We observed good numerical convergence and stability properties. In addition, we verified that the relationships

we imposed as boundary conditions were numerically satisfied and checked for mass conservation between the inlet and outlets. Subsequent to the verification studies, we solved a series of problems to demonstrate that realistic pressure fields could be computed and to compare and contrast impedance, resistance and constant pressure boundary conditions. This is described fully in the next section.

3. Results

In the examples below, the profile of the inlet velocity was chosen to be parabolic for subsequent comparisons with one-dimensional analysis simulations [18]. For a prescribed input flow, we do not expect that the pressure fields will be significantly different between time-varying parabolic and Womersley inlet boundary conditions. Furthermore, while the focus of this paper is on the outlet boundary conditions, the method described could be applied in a similar fashion for inlet boundary conditions to include, for example, a lumped model of the heart.

We first consider pulsatile flow in a straight vessel with a prescribed flow rate at the inlet mapped into a parabolic velocity profile and different boundary conditions at the outlet, to specifically observe the influence of the outlet boundary condition on the solution in the numerical domain. The inlet flow wave is a representative carotid flow rate [38,44,45]. The nominal radius of 0.3 cm and the vessel length of 12.6 cm (length to diameter ratio of 20) were chosen to correspond approximately to that of the human common carotid artery. The solution was computed on a 45,849 element and 9878 node mesh with a time step of 0.002 s, for a total of five cardiac cycles. The pressure pulse in the carotid artery has been reported to be approximately 70–80/110–120 mmHg for a healthy person [38,46]. The resistance value is the ratio of mean pressure to mean flow. The impedance is generated following Olufsen's approach described in the introduction: a fractal tree is generated starting from a vessel that matched the diameter of the outlet and diminished in size with each successive generation of vessels until a fixed terminal vessel size was attained. The length-to-radius ratio of the tree is chosen so that the zero-frequency of the impedance matches the previous resistance boundary condition. The mean outlet pressure of the previous simulations is chosen to impose the constant pressure outlet boundary condition. Fig. 3 depicts the results obtained with constant pressure, resistance and impedance outflow boundary conditions. Flow is displayed for reference, since the incompressibility constraint forces the flow to be instantaneously the same at the outlet as that prescribed at the inlet. The constant pressure outlet boundary condition results in a pressure pulse that does not have the correct amplitude or phase (pressure lags flow in reality). Note that this is the most common outlet boundary condition used for three-dimensional analyses of blood flow. The resistance boundary condition results in an unrealistically large pressure pulse, and forces pressure and flow to be in phase at the outlet. However, the resistance boundary condition is an improvement over the constant pressure outlet boundary condition when studying wave propagation, and does not require any knowledge of the pressure or flow wave forms before the simulation. Finally, Fig. 3 depicts the results for the impedance boundary condition. In this case, the pressure wave is propagated down the length of the vessel with little damping or dispersion. In this case, pressure lags flow and the pressure amplitude and wave form are similar to curves given by Nichols and O'Rourke [38]. Therefore, in regards to pressure curves, we conclude that the impedance boundary condition is the most realistic boundary condition examined.

To further illustrate the critical influence of boundary conditions, we performed numerical simulations in an idealized model of an abdominal aorta bifurcation to the iliac arteries with a 75% area reduction stenosis on one side, using realistic anatomic dimensions (see Fig. 4a) and inflow wave form for an abdominal aortic bifurcation. The finite element mesh consists of 94,280 elements and 19,579 nodes. A pulsatile, parabolic profile was imposed at the inlet, and constant pressure ($P = 90$ mmHg) or equal impedance boundary conditions (with a resistance of 24,000 dyn·s·cm^{-5}) at the two outlets. The simulation was run for 10 cardiac cycles, with a CFL number of 1 in the stenosis and thus a time step size of 0.0008 s, with three non-linear

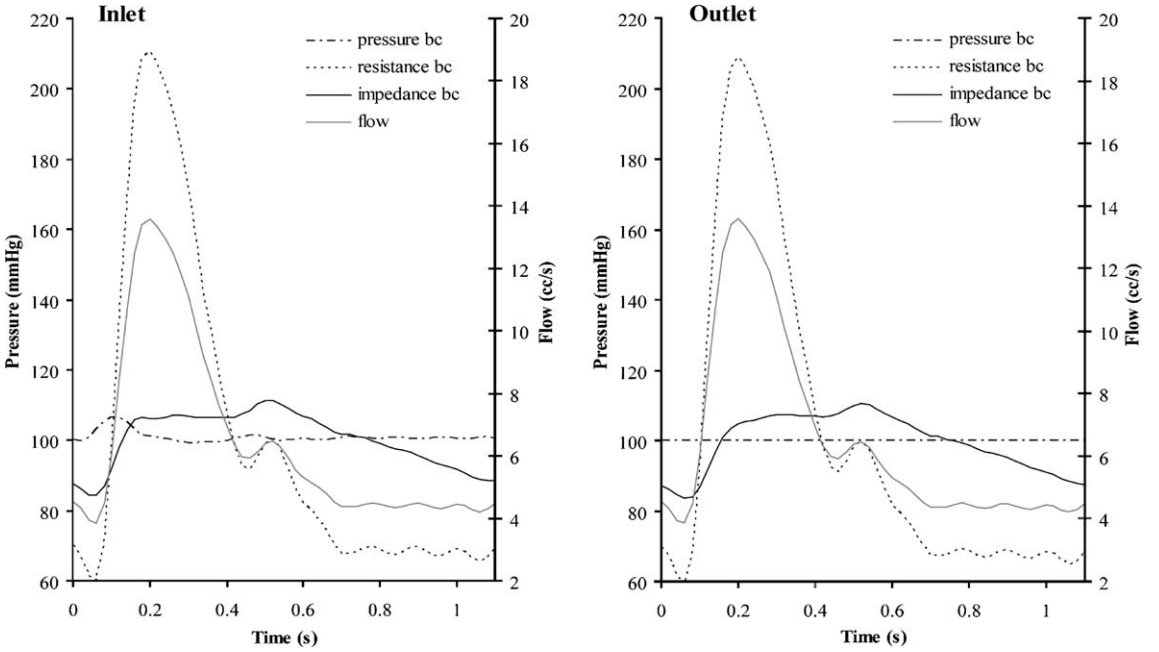

Fig. 3. Comparison of flow and pressure wave forms in a carotid artery with a periodic inlet flow and constant pressure, resistance and impedance outlet boundary conditions. For the pressure boundary condition, inlet pressure varies little from the prescribed constant outlet pressure and the peak pressure precedes the peak flow. The resistance boundary condition gives rise to an unrealistically large pressure amplitude. In addition, pressure and flow are in phase at the outlet. For the impedance boundary condition, the range of pressure is from approximately 85–115 mmHg and the pressure lags flow along the length of the vessel. 1 mmHg = 133.3 Pa, 1 cc/s = 10^{-6} m^3/s.

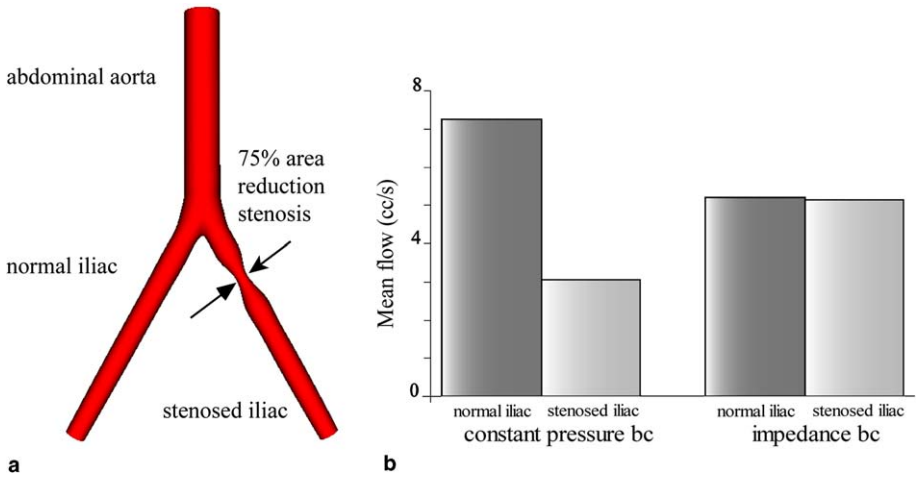

Fig. 4. (a) Geometric model and (b) flow distribution between normal iliac artery and an iliac artery with a stenosis that reduces the cross-sectional area by 75% for constant pressure and impedance boundary conditions. For a constant outlet pressure, the flow split is dictated solely by the resistance to flow due to the geometry of the computational domain (approximately 70% to the normal side, 30% to the stenosed side). For an impedance boundary condition with a physiologic level of resistance, the flow split (50%/50%) is principally determined by the downstream demands (represented by equal outlet impedances). These results are consistent with clinical observations for resting flow conditions and iliac artery stenoses with less than an 85% area reduction.

iterations per time step. Fig. 4b depicts the dramatic differences in flow split depending on outlet boundary conditions. With a constant outlet pressure, the flow split is dictated solely by the resistance to flow due to the geometry of the computational domain (70% flow to the normal side, 30% to the stenosed side). With an impedance boundary condition, the flow split (50%/50%) is primarily determined by the downstream conditions (represented by equal outlet impedances), which is representative of most clinical cases (i.e. for stenoses with less than an 85% area reduction). Note that because the impedance boundary condition incorporates the history of flow and pressure over a cardiac cycle, it takes longer for the solution to become periodic (about 6 cycles) than that observed with a constant outlet pressure (within 2 cycles).

The time varying flow and pressure curves at the inlet and outlets for the constant pressure and impedance boundary conditions are shown in Fig. 5. With the constant pressure boundary condition, blood flow

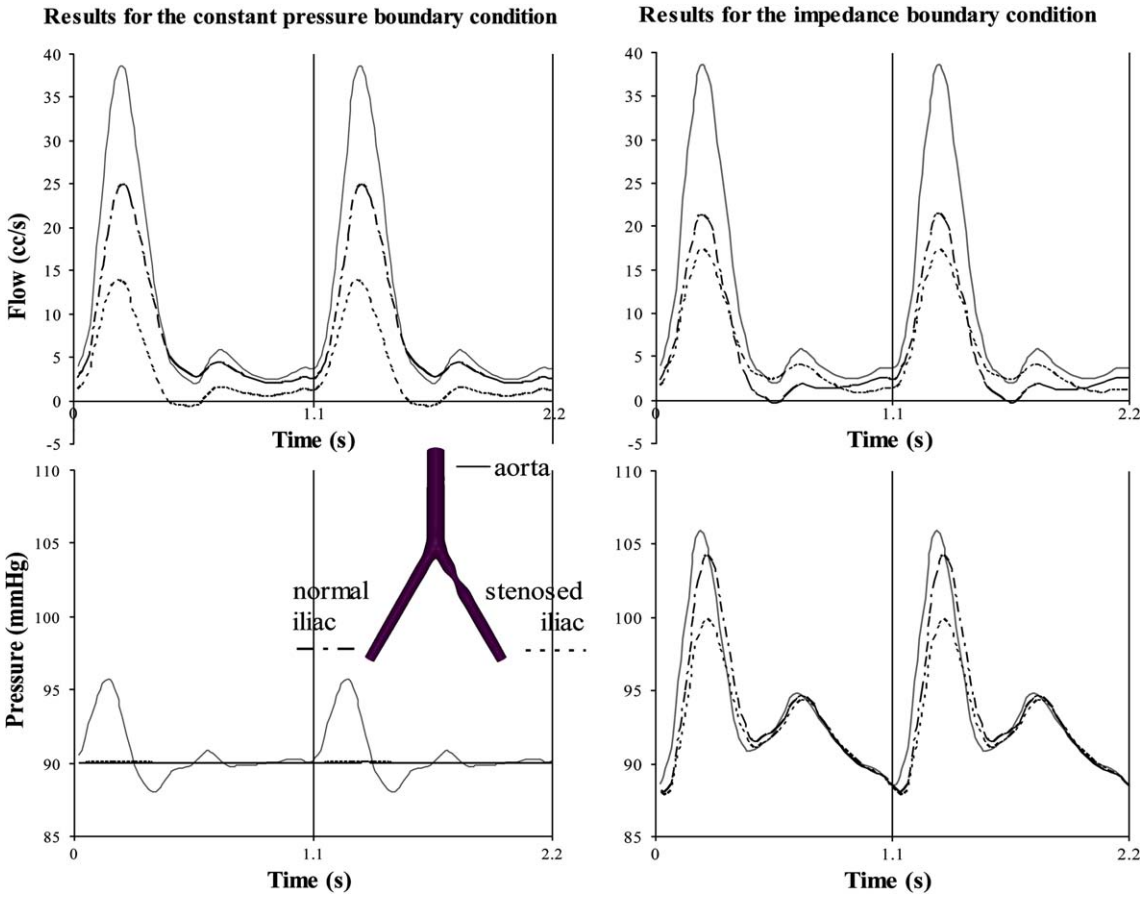

Fig. 5. Inlet and outlet flow and pressure curves during the last two cardiac cycles of the simulation for constant pressure (90 mmHg) and impedance outlet boundary conditions. Note that for the constant pressure boundary condition, the flow to the normal iliac artery exceeds that through the stenosed iliac artery for all time points in the cardiac cycle and the inlet pressure varies from approximately 88–96 mmHg. For the impedance outlet boundary condition, the peak flow is greater in the normal iliac artery than the stenosed iliac artery, yet during late systole and early diastole, the flow is greater in the stenosed iliac artery than the normal iliac artery. Note that for the impedance outlet boundary condition, the peak pressure for the normal iliac artery is close to that of the inlet pressure, whereas the peak pressure for the stenosed iliac artery is significantly less than that in the normal iliac artery. Also note that the inlet pressure varies between approximately 88 and 106 mmHg. 1 mmHg = 133.3 Pa, 1 cc/s = 10^{-6} m^3/s.

from the aorta to the normal iliac artery is greater than that to the stenosed iliac artery throughout the cardiac cycle, following the 70/30 mean flow split noted above. The inlet pressure amplitude for the pressure boundary condition is not representative of physiologic conditions: it is solely determined by the instantaneous pressure gradient from the inlet to the prescribed constant outlets that is needed to drive the flow to both outlets, and therefore is only a slight variation from the mean value. For the impedance boundary condition we observe that while the mean flow split is nearly 50/50, the normal iliac artery gets more flow at peak systole (when the effect of the 75% area stenosis is greatest) and less flow during diastole. We also note that for a brief period in diastole, the flow in the stenosed iliac artery is actually greater than the inlet flow, indicating flow is actually drawn from the normal iliac artery—coinciding with the brief period of reverse flow in the normal iliac artery. This latter observation is quite interesting and perhaps due to the fact that during the deceleration phase in late systole, blood is more easily decelerated in the normal iliac artery than would be expected for the stenosed iliac artery. Again, note that this phenomenon is not observed with constant outlet pressure boundary conditions. For the impedance boundary conditions, the inlet, normal iliac and right iliac pressure wave forms exhibit physiologic amplitudes and phase. Note that the peak systolic pressure at the outlet of the stenosed iliac artery is considerably less than that observed in the normal iliac artery and that all the pressure waveforms exhibit little difference in diastole when the flow rate is low.

Fig. 6 provides a dramatic illustration of the differences in the velocity fields between the constant pressure and impedance outlet boundary conditions. Velocity magnitude at peak systole and early diastole is shown along the symmetry plane of the model. The velocity fields for the two different outlet boundary conditions exhibit substantial differences. We note, in particular, that the peak velocity through the stenosis is much higher for the simulation performed with the impedance outlet boundary condition as compared to that performed with the constant pressure outlet boundary condition. This is consistent with the significant differences in flow through the stenosed iliac artery for the two boundary condition cases examined. Fig. 7 depicts the instantaneous pressure fields for the constant pressure and impedance outlet boundary conditions at peak systole and early diastole. Note the fact that the scales are different for the two boundary conditions and the two time points in the cardiac cycle examined.

Finally, we consider pulsatile flow in a model of the abdominal aorta of a normal subject with geometry and flow rates generated from magnetic resonance imaging data [47]. The measured volumetric flow rate at the level of the diaphragm was specified at the inlet boundary and impedances are specified at all the outlets. The exit impedances were chosen so that the mean flow rate in each of the branches corresponded to the measured flow distribution when such data was available and literature data as needed [48,49]. Fig. 8 shows the 3D model. A total of 800,151 elements and 167,850 nodes were utilized and the solution was computed using a time step of 0.001 s for a total of five cardiac cycles. Fig. 8 depicts the volume flow rate and pressure at the inlet and representative outlets of the subject-specific abdominal aorta model when impedance boundary conditions are applied. Blood flows into the different arteries according to the prescribed impedances representing the demands of the downstream trees. Previous simulations of pulsatile flow in the human abdominal aorta [50] were performed by imposing outflow velocity profiles using Womersley's theory of pulsatile flow in rigid vessels to match the prescribed volumetric flow rates. For the branch vessels feeding the viscera (celiac, superior mesenteric, inferior mesenteric and renal arteries), these flow rates were scaled to some fraction of the inlet flow waveform and reverse flow in the iliac arteries during diastole arose because more flow was pulled from the other branch vessels than was input to the abdominal aorta. Note that for the present simulations the flow split between the branch vessels occurs naturally. Finally, to illustrate the results that can be obtained from coupling three-dimensional simulations of blood flow to impedance boundary conditions, the mean wall shear stress for the subject-specific model is presented in Fig. 9. Clearly, mean wall shear stress will be highly affected by the outlet boundary conditions.

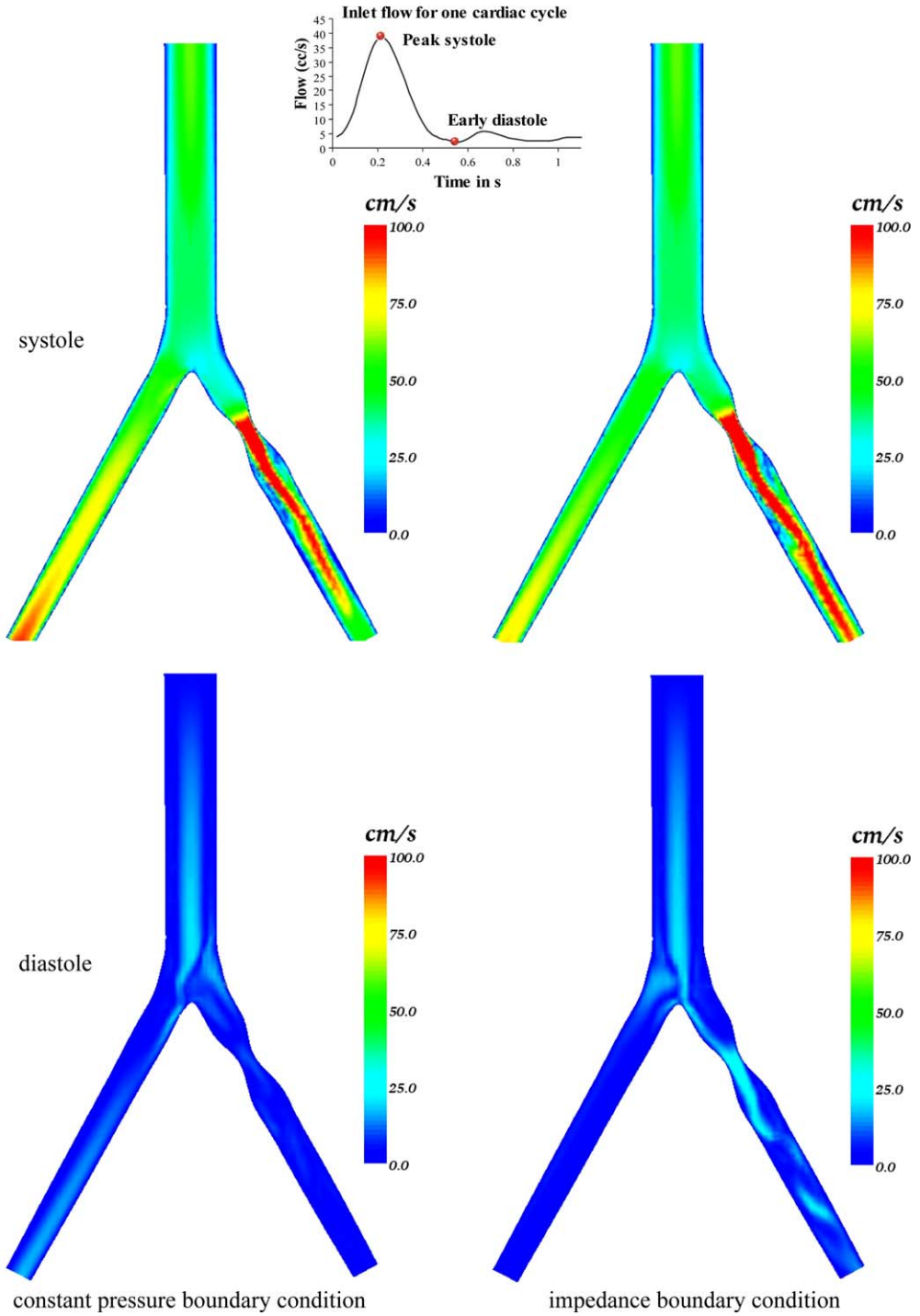

Fig. 6. Velocity magnitude along the symmetry plane of the model at peak systole and early-diastole for the constant pressure and impedance outlet boundary conditions.

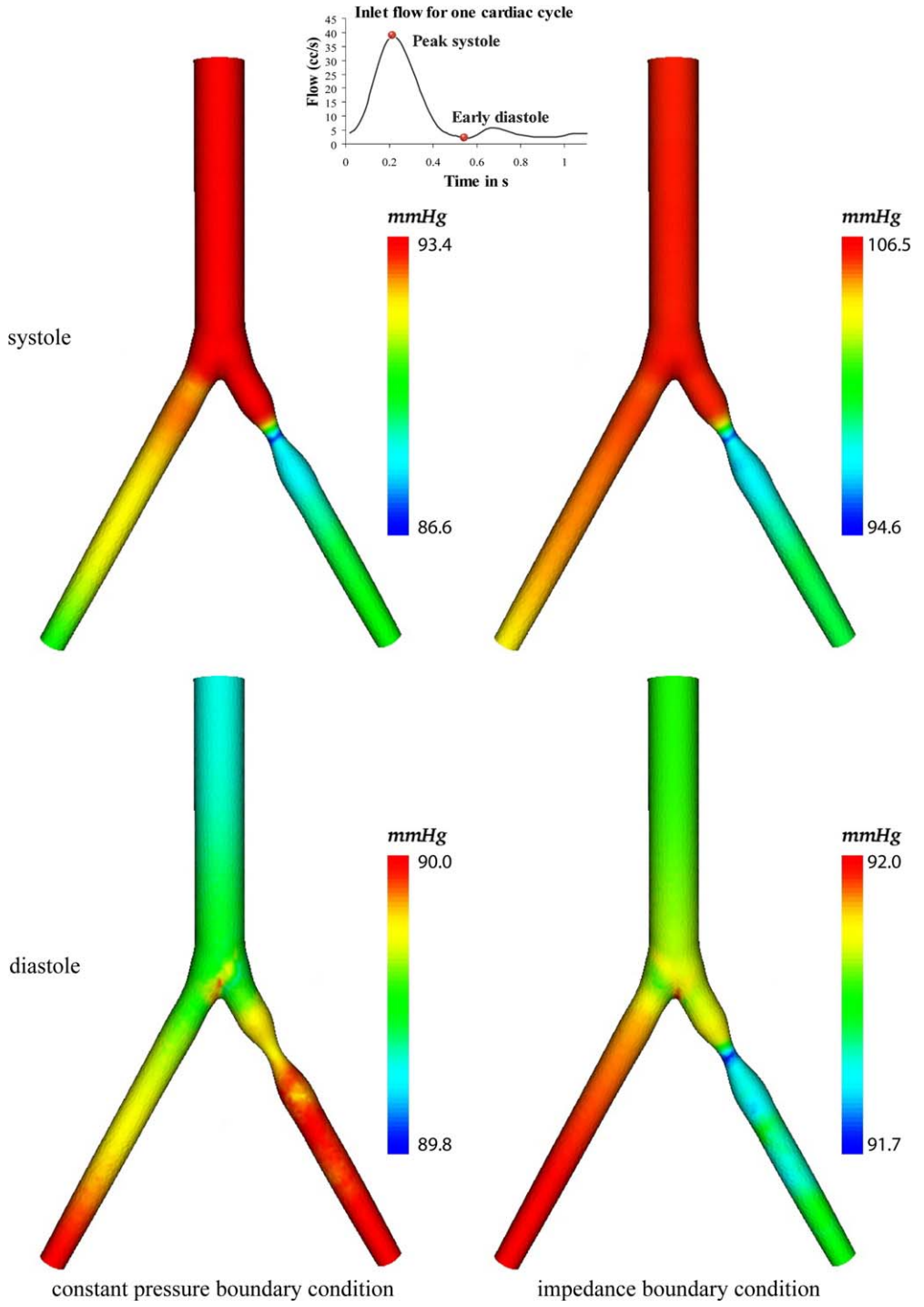

Fig. 7. Pressure at peak systole and early diastole for the constant pressure and impedance outlet boundary conditions. 1 mmHg = 133.3 Pa.

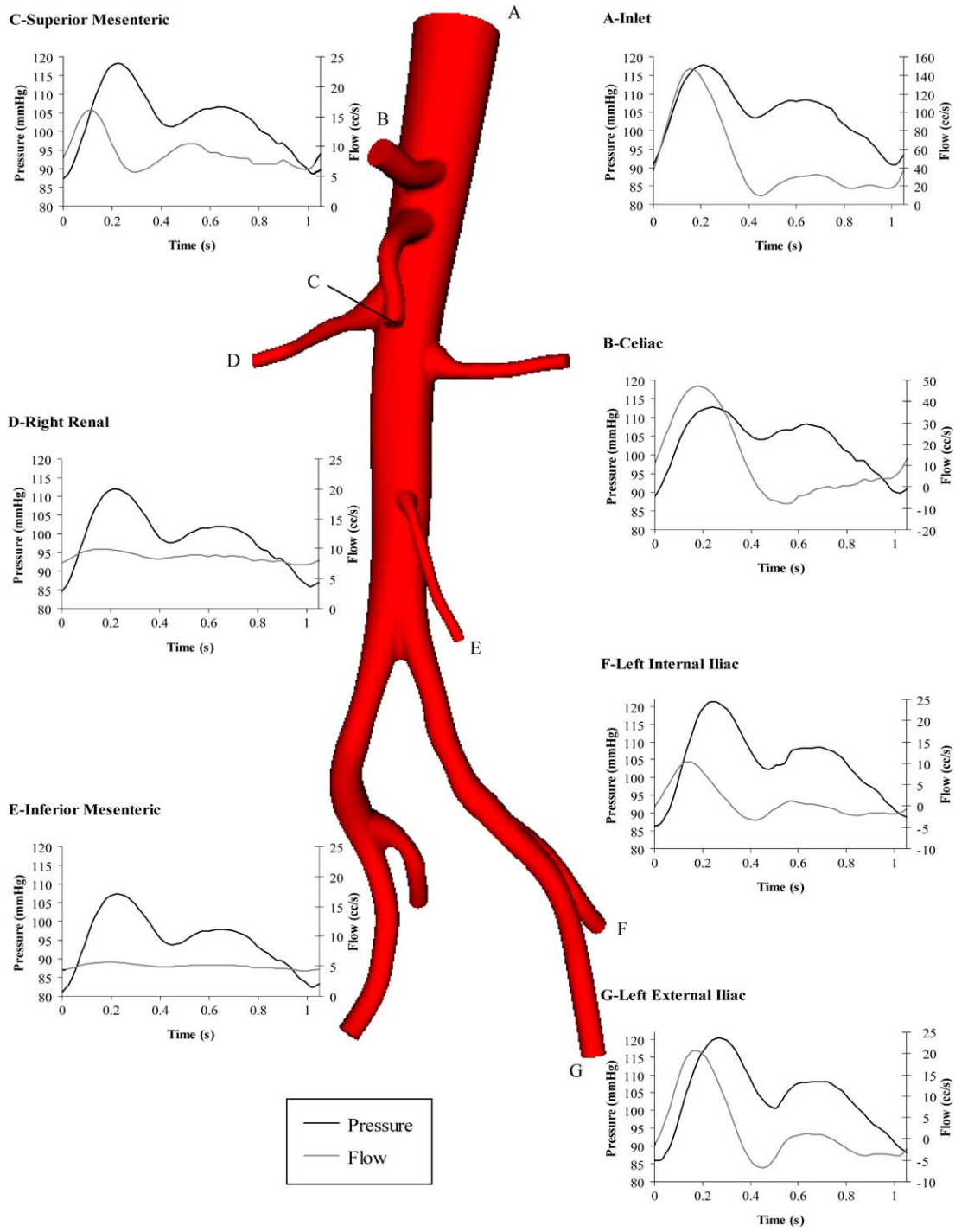

Fig. 8. Pressure and flow wave forms in a subject-specific model of the human abdominal aorta with a measured periodic inlet flow rate and impedance outlet boundary conditions. 1 mmHg = 133.3 Pa, 1 cc/s = 10^{-6} m^3/s.

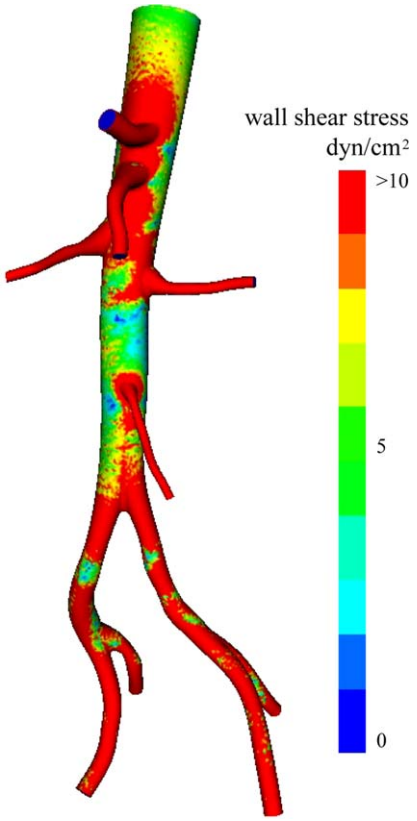

Fig. 9. Mean wall shear stress over one cardiac cycle for the subject-specific abdominal aorta model depicted in Fig. 8. 1 dyn/cm^2 = 0.1 Pa.

4. Conclusions

We have successfully developed and implemented a method to prescribe outflow boundary conditions intended for three-dimensional finite element simulations of blood flow based on the Dirichlet-to-Neumann and variational multiscale methods. As long as the effect of the downstream domain can be represented by an explicit function of pressure as a function of flow rate or velocity, the methods described can be used to couple the upstream three-dimensional numerical domain with the downstream analytic domain. The numerical results presented demonstrate that physiologic values of pressure can be attained and illustrate the importance of using appropriate boundary conditions. A long straight cylindrical blood vessel is used to demonstrate that realistic blood pressures can be calculated using this new method and that the choice of the outlet boundary conditions has a significant effect on the computed pressure field. The next example, an otherwise symmetric model of an abdominal aortic bifurcation with an obstruction in one iliac, demonstrates that the choice of outlet boundary conditions can dramatically affect the flow distribution, velocity and pressure fields. The final example, a patient specific abdominal aorta model, demonstrates that this approach can be used for complex multi-branched systems.

Results have been shown for idealized and patient specific 3D geometries, using physiological values, coupled to more sophisticated downstream models that incorporate memory-effects like the impedance boundary condition. Lumped parameter models more complex than a simple resistance could be easily incorporated in a manner similar to that used for the impedance boundary condition.

The stability of the solutions proved to be sensitive to the number of frequencies used to generate the impedance boundary condition, due to the convolution with the flow rate history. Although these results are very encouraging, for a more realistic representation of flow and pressure further analysis of the generation and validation of the impedance functions is needed. The impedance functions were generated using a binary fractal tree that did not incorporate differences between the branching patterns in different organs. Alternate models based on physical measurements of branching patterns would aid in the specification of realistic impedance functions. A further limitation of the impedance boundary condition is that it is derived based on the assumption of periodicity. An alternate outflow boundary condition that incorporates transient, non-periodic flows or a coupling to the non-linear one-dimensional equations of blood flow may be needed for non-periodic three-dimensional flow problems.

It is important to note that the present implementation does not incorporate deformable vessels in the three-dimensional domain and, as such, does not model wave propagation from the three-dimensional to one-dimensional domains. However, the analyses performed clearly indicate the need for appropriate boundary conditions in computing pulse pressures. Realistic values of blood pressure (mean and pulse) will be essential for obtaining accurate loading and displacement in fluid-solid interaction methods. Finally, the method described may be extensible to other biological and non-biological flow phenomena where the downstream model can be described as a function that links the primary variables or their derived quantities at the coupling interface.

Acknowledgements

This material is based upon work supported by the National Science Foundation under Grant No. 0205741 and a predoctoral fellowship from the American Heart Association. The authors gratefully acknowledge Dr. Mette Olufsen for the use of her methods to compute input impedance of vascular trees and Dr. Farzin Shakib for his linear algebra package (http://www.acusim.com). Finally, the authors gratefully acknowledge the assistance of Dr. Nathan Wilson for assistance with software development, Dr. Mary Draney for acquiring the subject-specific abdominal aorta MRI data, and Hyun Jin Kim for constructing the abdominal aorta model.

References

[1] C.A. Taylor, M.T. Draney, Experimental and computational methods in cardiovascular fluid mechanics, Ann. Rev. Fluid Mech. 36 (2004) 197–231.
[2] A. Kamiya, T. Togawa, Adaptive regulation of wall shear stress to flow change in the canine carotid artery, Am. J. Physiol. 239 (1) (1980) H14–H21.
[3] H. Wolinsky, S. Glagov, Comparison of abdominal and thoracic aortic medial structure in mammals. Deviation of man from the usual pattern, Circulation Res. 25 (6) (1969) 677–686.
[4] S. Glagov, C.K. Zarins, D.P. Giddens, D.N. Ku, Hemodynamics and atherosclerosis. Insights and perspectives gained from studies of human arteries, Arch. Pathol. Lab. Med. 112 (10) (1988) 1018–1031.
[5] C.K. Zarins, C.A. Taylor, Hemodynamic Factors in Atherosclerosis. Vascular surgery: A Comprehensive Review, W.S. Moore and W.B.S. Company, 2002, pp. 105–118.
[6] C.A. Taylor, M.T. Draney, J.P. Ku, D. Parker, B.N. Steele, K. Wang, C.K. Zarins, Predictive medicine: computational techniques in therapeutic decision-making, Comput. Aided Surgery 4 (5) (1999) 231–247.
[7] National Heart, Lung and Blood Institute report of the task force on research in pediatric cardiovascular disease, US Department of Health and Human Services, Public Health Service, National Institutes of Health, 2002.
[8] N. Stergiopulos, D.F. Young, T.R. Rogge, Computer simulation of arterial flow with applications to arterial and aortic stenoses, J. Biomech. 25 (12) (1992) 1477–1488.
[9] L. Formaggia, F. Nobile, A. Quarteroni, A. Veneziani, Multiscale modelling of the circulatory system: A preliminary analysis, Comput. Visualization Sci. 2 (2/3) (1999) 75–83.

[10] J. Wan, B.N. Steele, S.A. Spicer, S. Strohband, G.R. Feijoo, T.J.R. Hughes, C.A. Taylor, A one-dimensional finite element method for simulation-based medical planning for cardiovascular disease, Comput. Methods Biomech. Biomed. Engrg. 5 (3) (2002) 195–206.
[11] W.H. Ruan, M.E. Clark, M.D. Zhao, A. Curcio, A hyperbolic system of equations of blood flow in an arterial network, SIAM J. Appl. Math. 64 (2) (2003) 637–667.
[12] S.J. Sherwin, L. Formaggia, J. Peiro, V. Franke, Computational modelling of 1D blood flow with variable mechanical properties and its application to the simulation of wave propagation in the human arterial system, Int. J. Numer. Methods Fluids 43 (6–7) (2003) 673–700.
[13] J.R. Womersley, Oscillatory motion of a viscous liquid in a thin-walled elastic tube—I: the linear approximation for long waves, The Philos. Mag. 7 (1955) 199–221.
[14] J.R. Womersley, Oscillatory flow in arteries: the constrained elastic tube as a model of arterial flow and pulse transmission, Phys. Med. Biol. 2 (1957) 178–187.
[15] M.G. Taylor, Wave transmission through an assembly of randomly branching elastic tubes, Biophys. J. 6 (1966) 697–716.
[16] M.S. Olufsen, Structured tree outflow condition for blood flow in larger systemic arteries, Am. J. Physiol. 276 (1999) H257–H268.
[17] B.N. Steele, C.A. Taylor, Simulation of blood flow in the abdominal aorta at rest and during exercise using a 1-D finite element method with impedance boundary conditions derived from a fractal tree, in: Proceedings of the 2003 ASME Summer Bioengineering Meeting, Key Biscayne, FL, 2003.
[18] I. Vignon, C.A. Taylor, Outflow boundary conditions for one-dimensional finite element modeling of blood flow and pressure waves in arteries, Wave Motion 39 (4) (2004) 361–374.
[19] J.R. Cebral, M. Castro, O. Soto, R. Lohner, P.J. Yim, N. Alperin, Finite element modeling of the circle of Willis from magnetic resonance data, Proceedings of SPIE—The International Society for Optical Engineering 5031 (2003) 11–21.
[20] M. Oshima, R. Torii, T. Kobayashi, N. Taniguchi, K. Takagi, Finite element simulation of blood flow in the cerebral artery, Comput. Methods Appl. Mech. Engrg. 191 (6–7) (2001) 661–671.
[21] K. Perktold, G. Rappitsch, Computer simulation of local blood flow and vessel mechanics in a compliant carotid artery bifurcation model, J. Biomech. 28 (7) (1995) 845–856.
[22] J. Stroud, S. Berger, D. Saloner, Numerical analysis of flow through a severely stenotic carotid artery bifurcation, J. Biomech. Engrg. 124 (1) (2002) 9–20.
[23] G.R. Stuhne, D.A. Steinman, Finite-element modeling of the hemodynamics of stented aneurysms, J. Biomech. Engrg. 126 (3) (2004) 382–387.
[24] C.A. Taylor, T.J.R. Hughes, C.K. Zarins, Finite element modeling of blood flow in arteries, Comput. Methods Appl. Mech. Engrg. 158 (1998) 155–196.
[25] G. Pennati, F. Migliavacca, G. Dubini, R. Pietrabissa, M. de Leval, A mathematical model of circulation in the presence of the bidirectional cavopulmonary anastomosis in children with a univentricular heart, Med. Eng. Phys. 19 (3) (1997) 223–234.
[26] F. Migliavacca, M.R. de Leval, G. Dubini, R. Pietrabissa, R. Fumero, Computational fluid dynamic simulations of cavopulmonary connections with an extracardiac lateral conduit, Med. Engrg. Phys. 21 (3) (1999) 187–193.
[27] F. Migliavacca, P.J. Kilner, G. Pennati, G. Dubini, R. Pietrabissa, R. Fumero, M.R. de Leval, Computational fluid dynamic and magnetic resonance analyses of flow distribution between the lungs after total cavopulmonary connection, IEEE Trans. Biomed. Engrg. 46 (4) (1999) 393–399.
[28] E.B. Shim, R.D. Kamm, T. Heldt, R.G. Mark, Numerical analysis of blood flow through a stenosed artery using a coupled multiscale simulation method, Comput. Cardiol. (2000) 219–222.
[29] A. Quarteroni, S. Ragni, A. Veneziani, Coupling between lumped and distributed models for blood flow problems, Comput. Visualization Sci. 4 (2) (2001) 111–124.
[30] G. Guadagni, E.L. Bove, F. Migliavacca, G. Dubini, Effects of pulmonary afterload on the hemodynamics after the hemi-Fontan procedure, Med. Engrg. Phys. 23 (5) (2001) 293–298.
[31] K. Lagana, G. Dubini, F. Migliavacca, R. Pietrabissa, G. Pennati, A. Veneziani, A. Quarteroni, Multiscale modelling as a tool to prescribe realistic boundary conditions for the study of surgical procedures, Biorheology 39 (3–4) (2002) 359–364.
[32] A. Quarteroni, A. Veneziani, Analysis of a geometrical multiscale model based on the coupling of ODEs and PDEs for blood flow simulations, Multiscale Model. Simul. 1 (2) (2003) 173–195.
[33] K. Lagana, R. Balossino, F. Migliavacca, G. Pennati, E.L. Bove, M.R. de Leval, G. Dubini, Multiscale modeling of the cardiovascular system: application to the study of pulmonary and coronary perfusions in the univentricular circulation, J. Biomech. 38 (5) (2005) 1129–1141.
[34] L. Formaggia, J.F. Gerbeau, F. Nobile, A. Quarteroni, On the coupling of 3D and 1D Navier–Stokes equations for flow problems in compliant vessels, Comput. Methods Appl. Mech. Engrg. 191 (2001) 561–582.
[35] L. Formaggia, J. Gerbeau, F. Nobile, A. Quarteroni, Numerical treatment of defective boundary conditions for the Navier–Stokes equations, SIAM J. Numer. Anal. 40 (1) (2002) 376–401.
[36] D. Givoli, J.B. Keller, A finite element method for large domains, Comput. Methods Appl. Mech. Engrg. 76 (1) (1989) 41–66.

[37] T.J.R. Hughes, Multiscale phenomena: Green's functions, the Dirichlet-to-Neumann formulation, subgrid scale models, bubbles and the origins of stabilized methods, Comput. Methods Appl. Mech. Engrg. 127 (1995) 387–401.
[38] W.W. Nichols, M.F. O'Rourke, McDonald's Blood Flow in Arteries: Theoretical, Experimental and Clinical Principles, Oxford University Press, New York, 1998.
[39] P.M. Gresho, R.L. Sani, Incompressible Flow and the Finite Element Method, Wiley, 2000.
[40] A.N. Brooks, T.J.R. Hughes, Streamline upwind Petrov–Galerkin formulation for convection dominated flows with particular emphasis on the incompressible Navier–Stokes equations, Comput. Methods Appl. Mech. Engrg. 32 (1982) 199–259.
[41] L.P. Franca, S.L. Frey, Stabilized finite element methods II. The incompressible Navier–Stokes equations, Comput. Methods Appl. Mech. Engrg. 99 (2–3) (1992) 209–233.
[42] C.H. Whiting, K.E. Jansen, A stabilized finite element method for the incompressible Navier–Stokes equations using a hierarchical basis, Int. J. Numer. Methods Fluids 35 (2001) 93–116.
[43] K.E. Jansen, C.H. Whiting, G.M. Hulbert, Generalized-{alpha} method for integrating the filtered Navier–Stokes equations with a stabilized finite element method, Comput. Methods Appl. Mech. Engrg. 190 (3-4) (2000) 305–319.
[44] J.R. Cebral, R. Lohner, O. Soto, P.J. Yim, On the modelling of carotid blood flow from magnetic resonance images, in: Proceedings of the 2001 Summer Bioengineering Meeting, 2001.
[45] D.W. Holdsworth, C.J.D. Norley, R. Frayne, D.A. Steinman, B.K. Rutt, Characterization of common carotid artery blood-flow waveforms in normal subjects, Physiol. Meas. 20 (1999) 219–240.
[46] S.Z. Zhao, X.Y. Xu, A.D. Hughes, S.A. Thom, A.V. Stanton, B. Ariff, Q. Long, Blood flow and vessel mechanics in a physiologically realistic model of a human carotid arterial bifurcation, J. Biomech. 33 (8) (2000) 975–984.
[47] B.T. Tang, C.P. Cheng, P.S. Tsao and C.A. Taylor, Subject-specific finite element modeling of three-dimensional pulsatile flow in the human abdominal aorta: comparison of resting and exercise conditions, in: Proceedings of the 2003 Summer Bioengineering Meeting, Key Biscayne, FL, 2003.
[48] W.F.M. Ganong, Review of Medical Physiology, Appleton & Lange, Englewood Cliffs, 1995.
[49] A.C. Guyton, Physiology of the Human Body, Saunders College Publishing, San Francisco, 1984.
[50] C.A. Taylor, T.J.R. Hughes, C.K. Zarins, Finite element modeling of three-dimensional pulsatile flow in the abdominal aorta: relevance to atherosclerosis, Ann. Biomed. Engrg. 26 (6) (1998) 1–14.